AGU ADVANCING EARTH AND SPACE SCIENCE

Geophysical Research Letters

RESEARCH LETTER
10.1029/2020GL089209

# Pore Fluid Pressures and Strength Contrasts Maintain Frontal Fault Activity, Northern Hikurangi Margin, New Zealand

**Melodie E. French**[1] **and Julia K. Morgan**[1]

[1]Department of Earth, Environmental, and Planetary Sciences, Rice University, Houston, TX, USA

**Key Points:**
- The hanging wall of the Pāpaku fault is relatively strong due to tectonic stress history and lithification
- The foot wall and Pāpaku fault are relatively weak due to persistently elevated pore fluid pressures not inherent material properties
- High fluid pressure and low strength may be favorable for deformation partitioning within the foot wall and along the Pāpaku fault

**Supporting Information:**
- Text SI

**Correspondence to:**
M. E. French,
mefrench@rice.edu

**Citation:**
French, M. E., & Morgan, J. K. (2020). Pore fluid pressures and strength contrasts maintain frontal fault activity, northern Hikurangi margin, New Zealand. *Geophysical Research Letters*, *47*, e2020GL089209. https://doi.org/10.1029/2020GL089209

Received 9 JUN 2020
Accepted 25 OCT 2020
Accepted article online 30 OCT 2020



**Abstract** Diverse modes of fault slip occur within shallow subduction zones, but their relationships to upper plate deformation are poorly understood. IODP Expedition 375 collected samples and data across the northern Hikurangi margin, where tsunamigenic earthquakes and slow slip events occur. Site U1518 intersected the Pāpaku fault, a splay fault within the frontal accretionary wedge. To constrain in situ physical conditions and strength of the system, we conducted isotropic loading and triaxial compression experiments on hanging wall and foot wall cores and interpreted the results using critical state soil mechanics theory. The hanging wall is relatively strong, reflecting its tectonic history, whereas the foot wall and fault are anomalously weak owing to elevated pore pressure ($\lambda^* \geq 0.3$). Critical state in both samples corresponds to a friction coefficient of 0.6, constraining the strength of the Pāpaku fault. Low fault strength, maintained by excess pore pressures, suggests that the Pāpaku fault may still be active.

**Plain Language Summary** The greatest earthquake and tsunami hazards occur where one tectonic plate descends beneath another, known as a subduction zone. In some cases, the plates slip past one another at a slow continuous pace, and in others, they slip in punctuated bursts that produce earthquakes and sometimes tsunamis. In northern New Zealand, a segment of the subduction zone known as the Hikurangi margin experiences a combination of these slow and earthquake-producing slip modes. However, subduction plate boundaries may never reach Earth's surface, making the effects of their slip processes challenging to study. The Integrated Ocean Drilling Program (IODP) conducted two research cruises to drill boreholes, collect samples, and install instruments along the Hikurangi margin to better understand how and why the boundary slips. In a suite of laboratory experiments, we measured the strength of the rock recovered from one of the boreholes. Our results show that the strength is low due to the presence of high pressure fluids that fill the pore space of the rocks, which enables plate boundary deformation to propagate to the seafloor, potentially contributing to tsunami-generating earthquakes.

## 1. Introduction and Geologic Setting

The strength and longevity of faults control the partitioning of deformation within subduction zones, with fundamental implications for regional seismic hazards (Moore et al., 2007). The character of shallow fault slip is thought to be controlled by some combination of material properties, extrinsic conditions like pore fluid pressures, and system geometry (e.g., Cummins & Kaneda, 2000; Lotto et al., 2019; Moore & Saffer, 2001; Saffer, 2003; Saffer & Wallace, 2015). Although we have made considerable advancements in understanding fluid pressure environments of shallow accretionary prisms (Bassett et al., 2014; Kitajima, Chester, et al., 2012; Saffer et al., 2000; Screaton et al., 2002), fewer studies have focused on their mechanical properties (Flemings & Saffer, 2018; Gao et al., 2018; Karig, 1990; Kitajima & Saffer, 2014), which define the framework for deformation.

The megathrust fault beneath the northern Hikurangi margin hosts diverse modes of slip, including shallow slow slip events (SSEs) and tsunamigenic earthquakes (Doser & Webb, 2003; Wallace & Beavan, 2010; Wallace et al., 2016) (Figure 1a). During Integrated Ocean Drilling Program (IODP) Expeditions 372 and 375, four boreholes were drilled along a transect normal to this margin to collect core samples and data (Wallace et al., 2019). A primary objective was to constrain the physical and mechanical properties and stress regime of the upper plate to gain insights into the SSE source region.

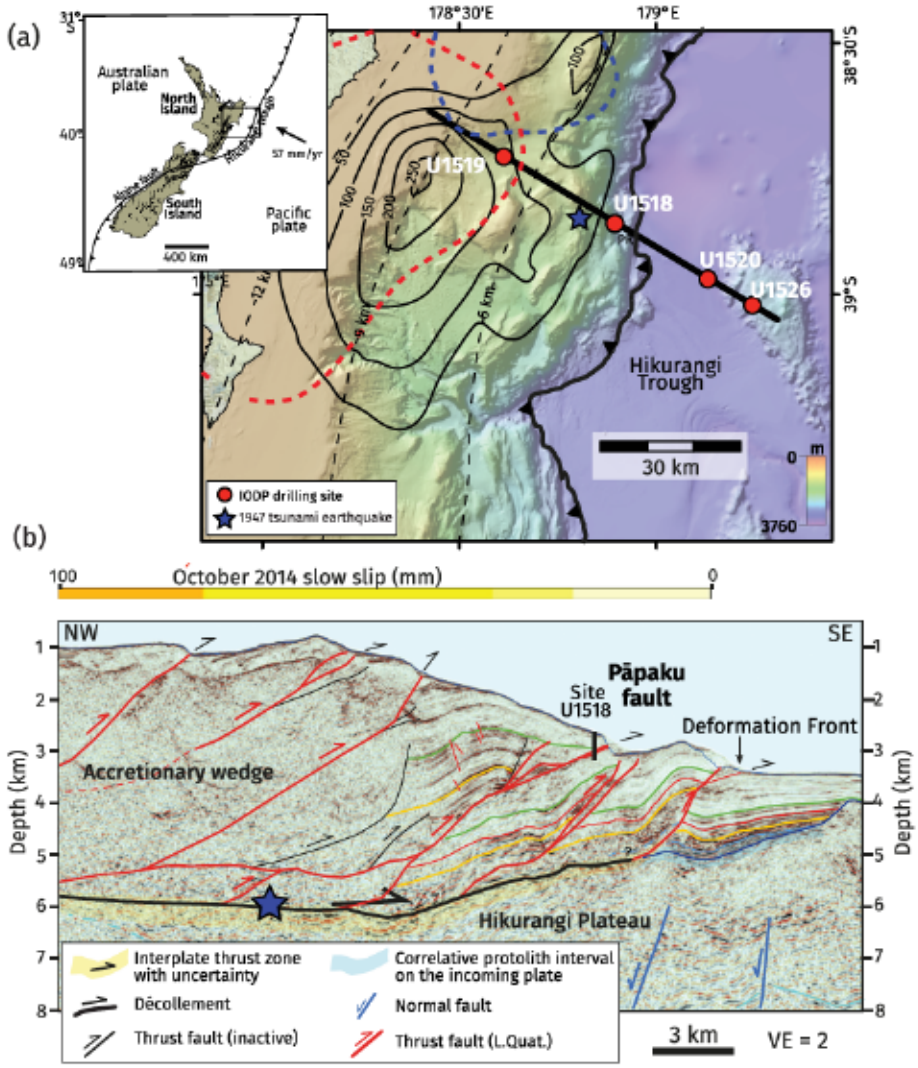


**Figure 1.** Setting of IODP Expeditions 372 and 375. (a) Bathymetric map (modified Figure 1a of Barnes et al., 2020). We investigate accretionary wedge sediments from drill Site U1518. Dashed black lines show depth to the plate interface (Williams et al., 2013), solid back lines show slip contours (mm) from a 2014 SSE, and dashed blue and red lines are the 40-mm slip contours for 2010 SSEs (Wallace et al., 2012, 2016). The blue star is the epicenter of a 1947 tsunami earthquake (Bell et al., 2014; Doser & Webb, 2003). (b) Seismic profile through Site U1518 and parallel to the transect in (a) (modified Figure 2a of Barnes et al., 2020). Structural interpretations were modified by Barnes et al. (2020) from Barker et al. (2018) and Saffer et al. (2019). The yellow bar shows the magnitude and horizontal extent of slip during the 2014 SSE (Wallace et al., 2016), and the blue star is the hypocenter of the 1947 tsunami earthquake (Doser & Webb, 2003; Wallace et al., 2016).

Along this margin, the Hikurangi plateau and ~1 km of sediments subduct beneath an accretionary prism composed of a 1–2 km thick sequence of accreted hemipelagic mudstones with interbedded sands, silts, and volcanic ash (Barnes et al., 2020). Site U1518 is located within the frontal accretionary wedge (Figure 1), and the borehole crossed the Pāpaku fault, a large splay fault that has accommodated ~6 km of offset and soles into the underlying megathrust (Fagereng et al., 2019) (Figure 1b). The fault dips landward and was penetrated at 304–322 mbsf, along with a subsidiary fault located at 351–361 mbsf (Figure 2a). It is not known, however, whether the fault is currently active and what roles it might play in accommodating plate convergence.

Shipboard porosities, $n$, at Site U1518 (Saffer et al., 2019) generally decrease with depth, from 0.60–0.70 near the seafloor to 0.40–0.45 just above Pāpaku fault (Figure 2b). However, porosity then steps up by ~0.05 within the Pāpaku fault and again within the subsidiary fault. Logging while drilling and regional seismic

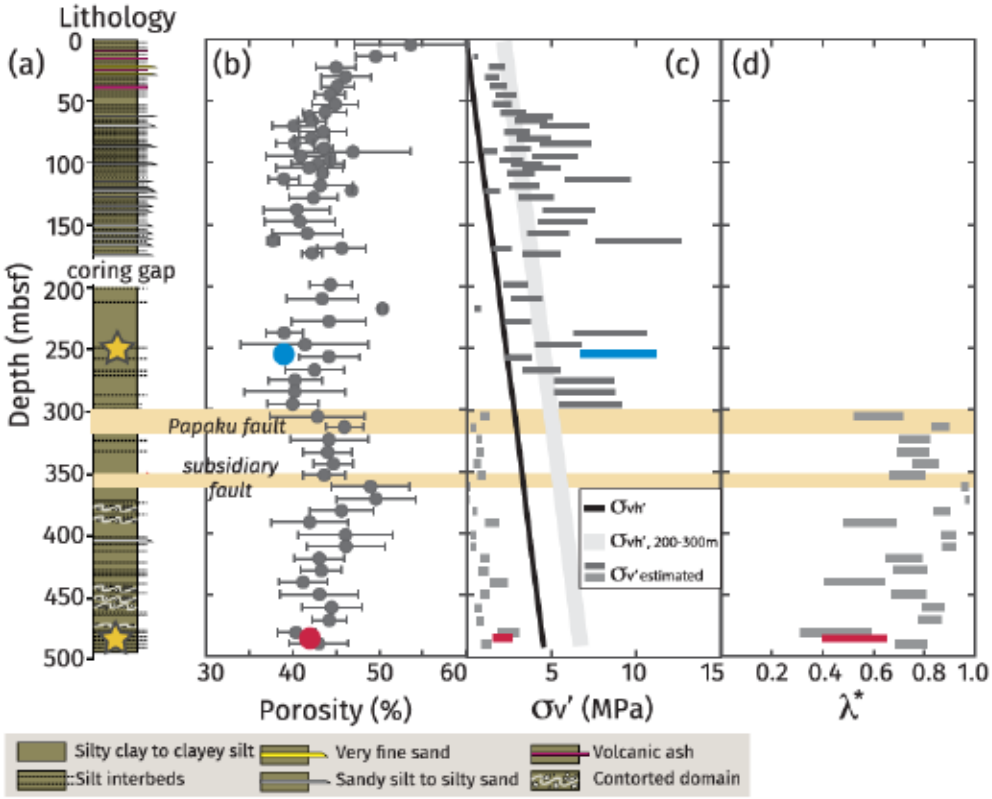


**Figure 2.** (a) Lithostratigraphy of Site U1518 from Saffer et al. (2019). Locations of our hanging wall and foot wall samples are shown with yellow stars (255 and 485 mbsf). (b) The porosities of our hanging wall (blue) and foot wall (red) samples and shipboard porosity measurements (dark gray). The average and standard deviation of shipboard porosity measurements for each core are shown. (c) The effective vertical stress with depth if fluid pressure is hydrostatic ($\sigma'_{Vh}$, black solid line) and the estimated paleoeffective vertical stress with hydrostatic fluid pressure before the erosion of 200 to 300 m overburden ($\sigma'_{Vh}$, 200–300 m, light gray line). The estimated range of $\sigma'_{Vu}$ that could result in the measured $p'_0$ values for our hanging wall (blue) and foot wall (red) samples their recovery depths. The estimated range of $\sigma'_{Vu}$ determined from shipboard porosity measurements for the hanging wall (dark gray) and foot wall (light gray). (d) The pore fluid pressure factor determined from shipboard porosity measurements in the foot wall and fault zones (light gray) and our experimental foot wall sample (red).

tomography velocities are consistent with lower porosities in the hanging wall than the foot wall (Cook et al., 2020; Gray et al., 2019; Saffer et al., 2019). Porosity and velocity variations may reflect variations in physical conditions or material properties across the Pāpaku and subsidiary fault zones. Structural observations showing evidence for significant ductile deformation in the fault zone and foot wall and predominantly brittle deformation in the hanging wall also indicate variations in physical properties and processes with depth (Fagereng et al., 2019). Anisotropy of magnetic susceptibility (AMS) fabrics indicate differences in the strain patterns of the hanging wall and foot wall that may help to explain differences in their physical properties (Greve et al., 2020).

We investigate the mechanical and pore pressure conditions at Site U1518 to understand the significance of these variations and their role in partitioning margin deformation. We use rock deformation experiments in combination with the extensive suite of density and porosity measurements made shipboard to constrain the rock strength and pore fluid pressure at Site U1518. Deformation experiments were conducted on intact samples from the hanging wall and foot wall of the Pāpaku fault and analyzed to estimate the strength and pore fluid pressure at sample depths. We then use the results of the deformation experiments and the properties measured shipboard from a larger suite of samples to estimate the strength and fluid pressure conditions with depth through the hanging wall, foot wall, and Pāpaku fault zone. These results have important implications for system evolution and how plate boundary slip is transferred to the margin toe.

## 2. Materials and Methods

We conducted deformation experiments on one hanging wall sample and one foot wall sample recovered from ~50 and ~160 m above and below the Pāpaku fault zone, respectively. X-ray diffraction (XRD) patterns of the two samples are very similar to each other and to nearby samples measured shipboard (Text S1 and Figure S1) (Saffer et al., 2019). Quantitative analyses of the XRD patterns measured from within 5 m of our samples and from the Pāpaku fault zone verify the similarities in composition (Table S1). We therefore infer that any differences in strength and deformation behavior of the experimental samples do not reflect differences in bulk mineralogy. The initial porosities, $n$, of our hanging wall and foot wall samples are 0.39 and 0.42, respectively, corresponding to void ratios, $e = n/(1-n)$, of 0.63 and 0.70 (Text S2).

Deformation experiments were conducted on cores 12.7 mm in diameter and 25–30 mm in length. Preparation of the cores revealed qualitative differences in mechanical properties of the samples. The hanging wall sample is cohesive and cores were prepared by shaving fragments into a cylindrical shape using a razor blade. In contrast, the foot wall sample is more compliant and cores were prepared by plunging Cu foil tubes into the sample, extracting the core, and then opening the foil and trimming the cores to length. All cores were prepared with their axes parallel to vertical.

We performed two isotropic compression and three triaxial compression tests under drained pore fluid conditions using a servo-controlled triaxial deformation apparatus (Text S3 and Figures S2 and S3a). For isotropic compression, confining ($\sigma_3$) and pore fluid ($P_f$) pressures were increased in steps of 0.25 MPa to an initial effective pressure ($\sigma_3 - P_f$) between 1 and 3 MPa. Next, confining pressure was increased to 32 MPa at 1 MPa/hour and subsequently decreased at the same rate while pore fluid pressure was held constant at 1 MPa. This constant stress rate led to a linear strain rate of $\dot{\epsilon_a} \approx 3$ to $7 \times 10^{-7}$ s$^{-1}$. Triaxial compression experiments were conducted at constant effective confining pressures of 1 and 5 MPa. The experiments were conducted by increasing the confining and pore fluid pressures to the initial conditions following the procedure used for isotropic loading. Samples equilibrated for 12 hours and the axial piston was then advanced at $10^{-8}$ m/s as effective confining pressure was held constant, resulting in an axial strain rate of $\dot{\epsilon_a} \approx 6 \times 10^{-7}$ s$^{-1}$, until an axial strain of 0.15.

## 3. Results

### 3.1. Mechanical Data

Isotropic compression results in a relationship between void ratio and effective pressure that is characteristic of sediment deformation (Figures 3a and 3b) (Bjerrum, 1967). If the sample has been previously consolidated, deformation is elastic at the lowest effective pressures and becomes plastic with increasing effective pressure. When effective pressure is reduced, some strain is recovered elastically. The slope of the line between $e$ and $\log_{10}(\sigma_3 - P_f)$ is the "elastic compression index," $C_e$, in the region of elastic deformation, which we measure during unloading (Figures 3a and 3b). The best fit to the linear region of plastic deformation is the "isotropic compression line," and its slope is the "plastic compression index," $C_c$ (Figures 3a and 3b). The isotropic compression line provides a relationship between void ratio and effective pressure during virgin isotropic consolidation. The transition between elastic and plastic deformation is the "isotropic yield strength," $p'_0$. We estimate $p'_0$ in two ways: as the intersection of linear fits to the elastic and plastic loading curves in a plot of $e$ versus the $\log_{10}(\sigma_3 - P_f)$, as well as the more elaborate Casagrande method (Casagrande, 1936). We find that $p'_0$ is significantly higher for the hanging wall ($6.7 \pm 0.2$ MPa) than foot wall ($1.6 \pm 0.3$ MPa) sample.

During triaxial compression at 1 MPa effective pressure, the hanging wall sample strain hardened to a peak strength and then strain weakened to an approximately steady-state strength (Figure 3c). This sample developed shear fractures in conjugate orientations, which combined with the observed strain weakening is characteristic of brittle deformation. In contrast, at both 1.2 and 5 MPa effective pressure, the foot wall sample strain hardened and deformation was distributed, indicating ductile deformation. The yield strength during triaxial compression was determined as the deviation from linearity during strain hardening. All samples exhibit net compaction throughout deformation (Figure 3d).

### 3.2. Strength Envelopes

We interpret the mechanical data using critical state soil mechanics theory, which relates sediment strength and mode of deformation (brittle or ductile) to its stress history (Figure 4a) (Karig & Hou, 1992;

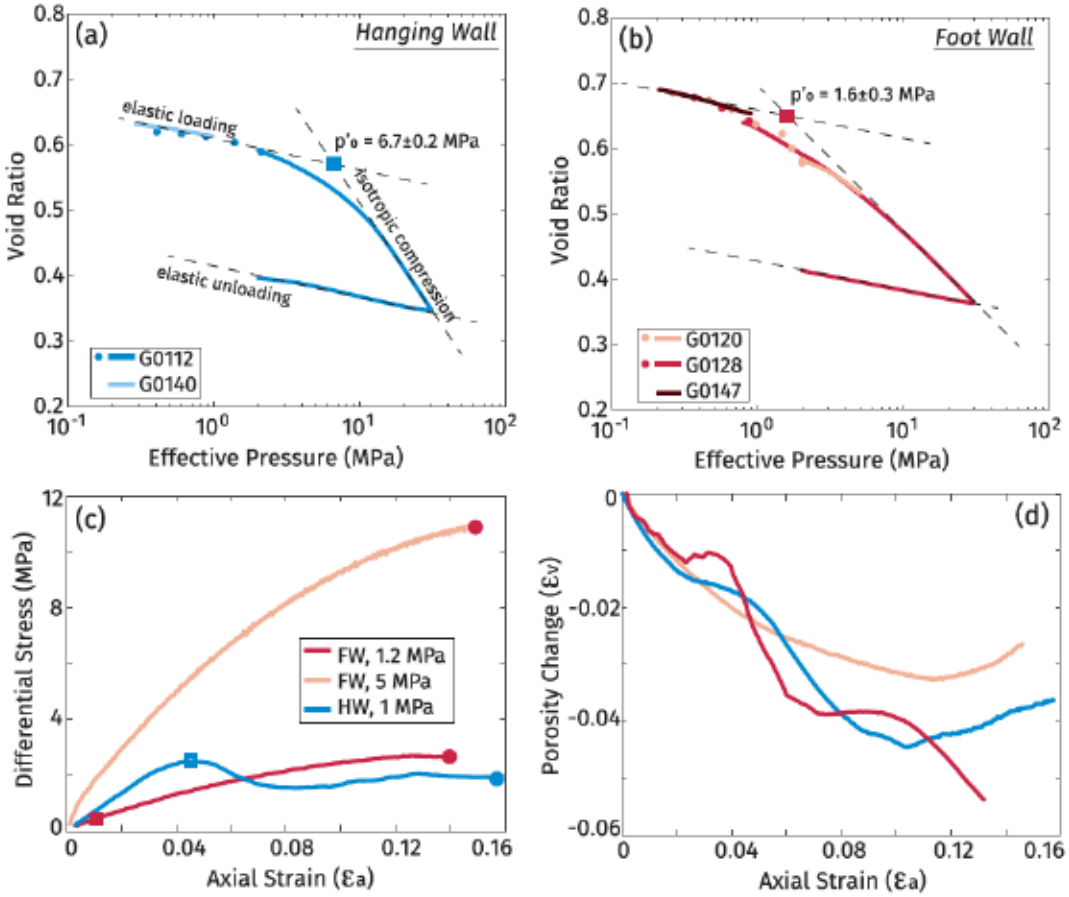


**Figure 3.** The relationship between void ratio and effective pressure for isotropic loading of (a) hanging wall and (b) foot wall samples. The intersection of linear fits to elastic loading and primary consolidation provides an estimate of the isotropic yield strength ($p_0'$, squares). The slope of elastic loading and unloading lines are assumed equal, and elastic loading is approximated by fitting the slope of the unloading line to the low stress data. This approximation is necessary as the elastic loading region is limited to very low stresses and thus more difficult to resolve than unloading. Error bars include uncertainty in the fit and the differences between this and the Casagrande methods (Casagrande, 1936). The evolution of (c) differential stress ($\sigma_1 - \sigma_3$) and (d) porosity change with axial strain during triaxial compression tests. Triaxial yield (hollow squares) and critical state (circles) strengths are shown with the same symbols in Figure 4b. Negative porosity change corresponds to compaction. Experimental conditions are in Table S2.

Muir Wood, 1991). In this framework, a yield envelope describes the onset of plastic deformation and has a concave shape in a stress space of differential stress ($q = \sigma_1 - \sigma_3$) versus effective mean stress ($p' = (\sigma_1 + 2\sigma_3)/3 - P_f$). Deformation is brittle where the yield envelope has a positive slope and ductile where it has a negative slope. Yield envelopes expand and strength increases with decreasing porosity, as occurs during progressive consolidation. For the stress paths of our triaxial compression tests, once the stress state reaches the yield envelope, strength evolves toward a "critical state" similar to the evolution toward a steady-state frictional strength in fault mechanics (Figure S3a).

In the triaxial compression experiments, the measured steady-state strengths are critical state strengths (Figure 3c). A best fit line through the critical state strength of all three triaxial compression experiments and the origin has a slope of $M = 1.25$ in $p' - q$ space (Figure 4b); considering the hanging wall and foot wall rocks separately does not change this result. We use the modified Cam-Clay (MCC) envelope as a convenient representation of the yield surface because it is determined only by $M$ and $p_0'$ (Roscoe & Burland, 1968); our experimentally determined $M$ and $p_0'$ values allow us to create MCC envelopes for the hanging wall and foot wall samples (Figure 4b). We note that these envelopes are only approximations for our materials because the MCC model assumes near-isotropic consolidation, which does not represent the deformation history at Site U1518 (Muir Wood, 1991). Nonetheless, the derived yield surface for the hanging wall is larger and illustrates that it is stronger than the foot wall, consistent with its lower porosity.

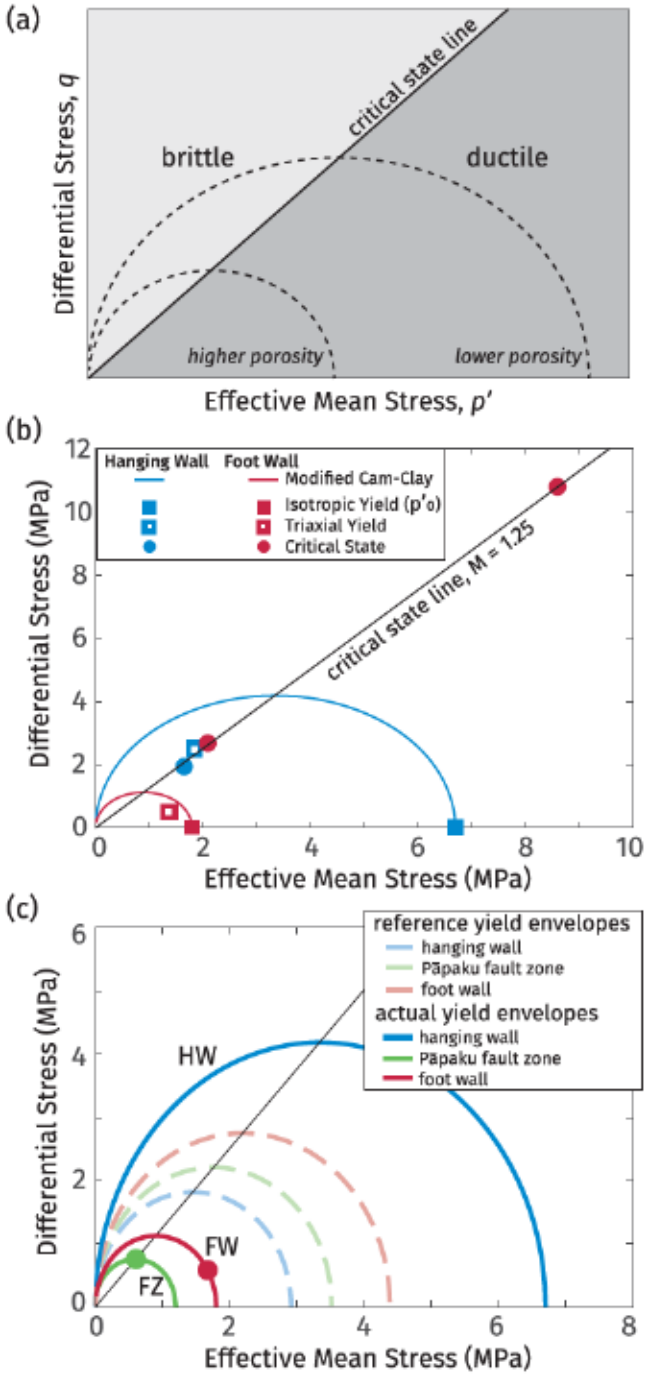


**Figure 4.** (a) Schematic critical state yield envelopes. Higher porosity rocks have a smaller yield envelopes and consolidation results in self-similar expansion of the envelope. The critical state line separates brittle (light gray) and ductile (dark gray) behavior. (b) Measured isotropic (solid squares) and triaxial (hollow squares) yield strengths and critical state strengths (circles) were determined from the data in Figure 3. The best fit critical state line is $q = 1.25p'$ ($R^2 = 0.99$). Strength envelopes for the MCC model ($\frac{q^2}{p'^2} + M^2\left(1 - \frac{p'_0}{p'}\right) = 0$ are shown. (c) The experimentally determined MCC envelopes for the hanging wall and foot wall and the estimated envelope for the fault zone are shown (solid lines) along with the reference yield envelopes expected if samples consolidated during uniaxial strain with hydrostatic pore fluid pressure (dashed lines). Circles show the approximate current stress states for the Pāpaku fault zone (FZ) and foot wall (FW).

## 4. Discussion

The fact that the hanging wall and foot wall samples can be fit with a single critical state line is consistent with their similar compositions (Figure 4b). However, their different isotropic compression lines suggest that the materials differ in other ways beyond the amount of consolidation they have experienced. Two effects may explain why the plastic compression index of the hanging wall sample is greater than that of the foot wall sample. First, lithification has been shown to increase the plastic compression index (Morgan & Ask, 2004), and the different methods required to prepare the experimental cores support more lithification of the hanging wall. Second, disturbance of a sample can reduce its plastic compression index (Burland, 1990; Skempton & Jones, 1944); thus, we cannot rule out that the foot wall sample experienced some disturbance during drilling. We take these factors into consideration below as we discuss the implications of the hanging wall and foot wall strengths for the current in situ stress state and deformation history of Site U1518.

### 4.1. Strength and Pore Fluid Pressure at Site U1518

Sediment that is deposited on the seafloor and consolidates under the weight of overburden is often approximated as having experienced a uniaxial strain path, whereby lateral strain is restricted by the adjacent sediment and consolidation occurs by vertical shortening (Atkinson & Bransby, 1982; Karig, 1990). To better understand the first-order deformation history at Site U1518, we use the uniaxial strain path as a reference and evaluate how the hanging wall and foot wall strengths differ from the predictions of this path under hydrostatic pore fluid pressure. Published uniaxial consolidation experiments and our own estimates show that, for uniaxially consolidated sediment, the effective vertical stress, $\sigma'_{Vu}$, can be approximated from the isotropic yield strength as $p'_0 \leq \sigma'_{Vu} \leq 1.7p'_0$ (Text S4) (Casey et al., 2015, 2016; Graham et al., 1983; Muir Wood, 1991). Our approach is to evaluate $\sigma'_{Vu}$ estimated from our measurements of $p'_0$ in the hanging wall and foot wall and compare these to the predicted in situ effective vertical stress assuming hydrostatic fluid pressure ($\sigma'_{Vh}$) (Figure 2b). We then discuss the tectonic and environmental factors that may have resulted in differences between the measured sediment strength (represented by $\sigma'_{Vu}$) and $\sigma'_{Vh}$.

For the hanging wall sample, $\sigma'_{Vu}$ is 2.8 to 4.7 times greater than $\sigma'_{Vh}$, indicating that the rock is stronger than expected from burial and consolidation at its current depth (Figure 2b). In contrast, for the foot wall sample, $\sigma'_{Vu}$ is 0.4 to 0.7 times $\sigma'_{Vh}$, indicating that it has experienced a maximum effective stress that is less than the weight of the overlying sediment with hydrostatic pore fluid pressure (Figure 2b).

Only two experimental samples were available for this study; however, to a first order, we can evaluate whether the relative strengths of the hanging wall and foot wall are consistent throughout Site U1518 using the shipboard porosity measurements. To do so, we assume that the isotropic compression lines measured from the hanging wall and foot wall samples are representative of the hanging wall and foot wall materials, respectively. In addition, given the compositional evidence that the Pāpaku and subsidiary fault zones are primarily derived from the foot wall with no evidence for chemical alteration or lithification (Saffer et al., 2019), we assume that the critical state and isotropic compression lines of the foot wall describe the fault zones as well. First, we use the isotropic compression lines to calculate $p'_0$ as a function of depth from the shipboard porosity measurements (Figures 2b and S4 and Text S5). We then estimate $\sigma'_{Vu}$ values from these $p'_0$ values (Figure 2c). Despite the considerable uncertainty in $\sigma'_{Vu}$ estimates using this approach, trends emerge in both the hanging wall and foot wall.

In the hanging wall, $\sigma'_{Vu}$ is consistently greater than $\sigma'_{Vh}$, similar to our experimental hanging wall sample (Figure 2c). There are several plausible explanations for this strength. Strengthening can occur because the present-day mean effective stresses are higher than for uniaxial strain conditions, as expected in a thrust faulting regime (Karig & Morgan, 1994). In addition, overconsolidation, wherein the sediments previously experienced higher stresses than exist at present, can cause greater strength than predicted for its depth. Indeed, between 200 and 300 m of sediment is believed to have slumped away at this site (Saffer et al., 2019), which could cause overconsolidation (Karig & Morgan, 1994). We estimate the effective vertical stress in the hanging wall prior to the removal of 200 to 300 m of overburden, however, and find that overconsolidation due to erosion does not clearly describe the data (light gray line in Figure 2c). Increased tectonic loading of the hanging wall earlier in the development of the thrust fault may also have contributed to its strength, although this effect is more difficult to quantify (Flemings & Saffer, 2018). Finally, some strengthening could result from lithification, consistent with the larger plastic compression index of the hanging wall

(Morgan & Ask, 2004). Because the hanging wall is stronger than predicted for uniaxial consolidation, we can infer processes that strengthen the rock but cannot estimate the current in situ pore fluid pressure.

In the foot wall and fault zones, $\sigma'_{Vu}$ is consistently lower than $\sigma'_{Vh}$, consistent with the experimental foot wall sample (Figure 2c). The best explanation for this result is that the pore fluid pressure in the foot wall and fault zones is and has always been greater than hydrostatic. The use of the stress state predicted from a uniaxial strain condition ($\sigma'_{Vu}$) as our reference is supported by magnetic fabrics recorded in the foot wall that indicate strain is primarily due to uniaxial gravitational loading (Greve et al., 2020), as well as previous studies that have shown dominantly uniaxial strain in the foot wall of accretionary splay faults (Karig & Morgan, 1994). We have assumed here that sediments within both the foot wall and fault zones have followed uniaxial strain paths, and thus, we can estimate the in situ fluid overpressure from our estimates of $p'_0$. We recognize that the fault zones have not followed a uniaxial strain path. Previous work suggests that this approximation may tend to underestimate the pore pressure in the fault zones (Flemings & Saffer, 2018). In particular, the fault zone is expected to have lower porosity than the foot wall for the same pore pressure. As a result, our estimates of $\lambda^*$ within the faults are likely underestimates.

We evaluate pore fluid pressurization using the pore pressure parameter $\lambda^* = (P_f - P_h)/(P_l - P_h)$ (Saffer & Tobin, 2011), where $P_h$ is hydrostatic fluid pressure, $P_l$ is lithostatic fluid pressure, and $P_f$ is the in situ fluid pressure, estimated as the difference between the total vertical stress and our estimates of the effective vertical stress, $\sigma'_{Vu}$ (Text S7). Values of $\lambda^*$ range from 0 to 1 for hydrostatic to lithostatic fluid pressure. In the foot wall, estimates of $\lambda^*$ are all greater than 0.3 and generally increase toward the fault zones (Figure 2d). Estimates of $\lambda^*$ from our experimental foot wall sample, on which a direct measurement of $p'_0$ was made, lie between 0.4 and 0.65. The lower bounds of our $\lambda^*$ estimates correspond to the upper bound of $\sigma'_{Vu}$, which equal to $1.7p'_0$; if we take these as conservative estimates of fluid pressurization, the pore fluid factors determined from shipboard porosity measurements lie between 0.5 and 0.9 within the fault zones. If the foot wall sample has been disturbed, the estimates of $p'_0$ and $\sigma'_{Vu}$ may be underestimates, in which case $\lambda^*$ may be overestimated. Furthermore, although variations in $\lambda^*$ estimates from adjacent samples likely reflect, in part, uncertainty in their values, our results consistently indicate elevated pore fluid pressures within the foot wall and fault zones. Given the low strengths of the foot wall and fault zones, the simplest explanation for the origin of high pore pressures is that they are locally derived due to incomplete consolidation and drainage of pre-existing pore fluids during burial.

### 4.2. Pāpaku Fault Strength

Structural observations of the core at Site U1518 indicate that the Pāpaku fault zone spans a thickness of ~57 m, with the greatest intensity of deformation within the upper 18 m interpreted as the main fault strand (Fagereng et al., 2019). The layer-parallel ductile shear fabric within the main fault denotes a mature fault, controlled by the yield surface of the fault rocks rather than the adjacent wall rocks. Thus, the stress within the fault zone is assumed to be at critical state, at the top of the MCC yield surface, a condition that is independent of the stress history of the material (Muir Wood, 1991). Importantly, because the yield surface is assumed to correspond to constant porosity independent of stress state, we can estimate the critical state strength in terms of differential stress, $q$, from our estimates of $p'_0$ in the fault zone using shipboard porosity measurements and our determination of $M = 1.25$. To do so, we construct a MCC envelope for the fault zone using the most conservative value of $p'_0$ determined from the shipboard porosity measurements of fault zone rocks (~1.3 MPa) corresponding to lower bound values of $\lambda^*$ (0.5) (Figures 2c, 2d, and 4c). We see that the MCC envelope of the fault zone intersects the critical state line at $q \approx 0.8$ MPa (Figure 4c). Although only an estimate given potential uncertainties in the isotropic compression line and use of MCC as the yield envelope, our results suggest that the maximum possible shear stress along the fault ($q/2$) may be as low as 0.4 MPa.

Fault strength is often represented using a frictional relation, whereby the friction coefficient, $\mu$, is a material property and the constant of proportionality between shear strength of the fault and the effective normal stress. Mature faults at steady state obey both this and the critical state relations, and thus, there is a direct relationship between $\mu$ and $M$ that is given by $\mu = \tan(\sin^{-1}(3M/(M+6)))$ (Muir Wood, 1991; Rutter & Glover, 2012). Our measured value of $M = 1.25$ results in $\mu = 0.6$. A friction coefficient of $\mu = 0.6$ is at the low end of Byerlee frictional strength (Byerlee, 1978) and is likely controlled by composition and the low effective stresses (e.g., Rabinowitz et al., 2018). Friction coefficient correlates with clay content (Tembe et al., 2010), and our measured value is similar to that of Nankai prism sediments having similar clay contents

(Song et al., 2011) and slightly higher than that of Nankai prism sediments with higher clay and phyllosilicate contents ($M = 0.75$ to 1.1 and $\mu = 0.35$ to 0.52) (Kitajima & Saffer 2012).

The frictional strength of the Pāpaku fault is not characteristic of a "weak" material. However, elevated pore fluid pressures in the fault zone characterized by $\lambda^*$ values approximated between 0.5 and 0.9 from shipboard porosity measurements (section 4.1) may permit fault slip at relatively low shear stress. Such low strength may have enabled the ~6 km of documented displacement along the fault (Fagereng et al., 2019) and is potentially favorable for present-day slip along the Pāpaku fault.

## 5. Conclusions

We conducted deformation experiments on samples from the hanging wall and foot wall of the Pāpaku fault, a thrust fault within the frontal accretionary wedge of the Hikurangi margin. We used these results to interpret porosity with depth profiles across the fault zone at IODP Expedition 375 Site U1518. We show that the enhanced strength of the hanging wall is consistent with tectonic loading during its complex history, likely with some subsequent lithification. In contrast, our results indicate that the foot wall and Pāpaku fault are weaker than the hanging wall owing to elevated pore fluid pressures and unaixial strain conditions in the foot wall. Although only first-order estimates, our results suggest that the fluid overpressure may increase toward and within the Pāpaku fault and a subsidiary fault zone, from an estimated pore pressure factor, $\lambda^*$, of ~0.3 to greater than 0.5. Thus, despite the fact that the critical state ($M = 1.25$) and frictional ($\mu = 0.6$) strengths of the rocks are not particularly low, the Pāpaku fault may deform at low shear stress owing to fluid overpressure. We conclude that these conditions may be generally favorable for ongoing slip along this frontal thrust.

## Data Availability Statement

The experimental data are available at the Rice Digital Scholarship archive (https://doi.org/10.25611/10pr-5804).

**Acknowledgments**
This work was funded by NSF EAR 1759127 to French and USSSP-IODP Subaward 66B(GG009393) of NSF Award OCE1450528 to Morgan. We thank Peter Flemings and an anonymous reviewer for helpful reviews of the manuscript and Ben Belzer for measuring the X-ray diffraction profiles.

## References

Atkinson, J., & Bransby, P. (1982). *The mechanics of soils: An introduction to critical state soil mechanics*. New York, NY: McGraw-Hill Book.

Barker, D. H. N., Henrys, S., Caratori Tontini, F., Barnes, P. M., Bassett, D., Todd, E., & Wallace, L. (2018). Geophysical constraints on the relationship between seamount subduction, slow slip, and tremor at the north Hikurangi subduction zone, New Zealand. *Geophysical Research Letters*, *45*, 12,804–12,813. https://doi.org/10.1029/2018GL080259

Barnes, P. M., Wallace, L. M., Saffer, D. M., Bell, R. E., Underwood, M. B., Fagereng, A., & LeVay, L. J. (2020). Slow slip source characterized by lithological and geometric heterogeneity. *Science Advances*, *6*(13), eaay3314. https://doi.org/10.1126/sciadv.aay3314

Bassett, D., Sutherland, R., & Henrys, S. (2014). Slow wavespeeds and fluid overpressure in a region of shallow geodetic locking and slow slip, Hikurangi subduction margin, New Zealand. *Earth and Planetary Science Letters*, *389*, 1–13. https://doi.org/10.1016/j.epsl.2013.12.021

Bell, R., Holden, C., Power, W., Wang, X., & Downes, G. (2014). Hikurangi margin tsunami earthquake generated by slow seismic rupture over a subducted seamount. *Earth and Planetary Science Letters*, *397*, 1–9. https://doi.org/10.1016/j.epsl.2014.04.005

Bjerrum, L. (1967). Engineering geology of Norwegian normally-consolidated marine clays as related to settlements of buildings. *Geotechnique*, *17*(2), 83–118.

Burland, J. B. (1990). On the compressibility and shear strength of natural clays. *Géotechnique*, *40*(3), 329–378. https://doi.org/10.1680/geot.1990.40.3.329

Byerlee, J. (1978). Friction of rocks. *Pure and Applied Geophysics*, *116*(4–5), 615–626.

Casagrande, A. (1936). The determination of pre-consolidation load and its practical significance. In *Proceedings of the International Conference on Soil Mechanics and Foundation Engineering* (Vol. 3, p. 60). Cambridge, Mass: Harvard University.

Casey, B., Germaine, J., Flemings, P., & Fahy, B. (2015). Estimating horizontal stresses for mudrocks under one-dimensional compression. *Marine and Petroleum Geology*, *65*, 178–186. https://doi.org/10.1016/j.marpetgeo.2015.02.001

Casey, B., Germaine, J. T., Flemings, P. B., & Fahy, B. P. (2016). In situ stress state and strength in mudrocks. *Journal of Geophysical Research: Solid Earth*, *121*, 5611–5623. https://doi.org/10.1002/2016JB012855

Cook, A. E., Paganoni, M., Clennell, M. B., McNamara, D. D., Nole, M., Wang, X., & Petronotis, K. E. (2020). Physical properties and gas hydrate at a near-seafloor thrust fault, Hikurangi margin, New Zealand. *Geophysical Research Letters*, *47*, e2020GL088474. https://doi.org/10.1029/2020GL088474

Cummins, P. R., & Kaneda, Y. (2000). Possible splay fault slip during the 1946 Nankai earthquake. *Geophysical Research Letters*, *27*(17), 2725–2728. https://doi.org/10.1029/1999GL011139

Doser, D. I., & Webb, T. H. (2003). Source parameters of large historical (1917–1961) earthquakes, North Island, New Zealand. *Geophysical Journal International*, *152*(3), 795–832. https://doi.org/10.1046/j.1365-246X.2003.01895.x

Fagereng, A., Savage, H., Morgan, J., Wang, M., Meneghini, F., Barnes, P., et al. (2019). Mixed deformation styles observed on a shallow subduction thrust, Hikurangi margin, New Zealand. *Geology*, *47*(9), 872–876. https://doi.org/10.1130/G46367.1

Flemings, P. B., & Saffer, D. M. (2018). Pressure and stress prediction in the Nankai accretionary prism: A critical state soil mechanics porosity-based approach. *Journal of Geophysical Research: Solid Earth*, *123*, 1089–1115. https://doi.org/10.1002/2017JB015025

Gao, B., Flemings, P. B., Nikolinakou, M. A., Saffer, D. M., & Heidari, M. (2018). Mechanics of fold-and-thrust belts based on geomechanical modeling. *Journal of Geophysical Research: Solid Earth*, *123*, 4454–4474. https://doi.org/10.1029/2018JB015434

Graham, J., Noonan, M. L., & Lew, K. V. (1983). Yield states and stress-strain relationships in a natural plastic clay. *Canadian Geotechnical Journal*, *20*(3), 502–516. https://doi.org/10.1139/t83-058

Gray, M., Bell, R. E., Morgan, J. V., Henrys, S., Barker, D. H. N., & the IODP Expedition 372 and 375 science parties (2019). Imaging the shallow subsurface structure of the north Hikurangi subduction zone, New Zealand, using 2-D full-waveform inversion. *Journal of Geophysical Research: Solid Earth*, *124*, 9049–9074. https://doi.org/10.1029/2019JB017793

Greve, A., Kars, M., Zerbst, L., Stipp, M., & Hashimoto, Y. (2020). Strain partitioning across a subduction thrust fault near the deformation front of the Hikurangi subduction margin, New Zealand: A magnetic fabric study on IODP Expedition 375 Site U1518. *Earth and Planetary Science Letters*, *542*, 116322. https://doi.org/10.1016/j.epsl.2020.116322

Karig, D. E. (1990). Experimental and observational constraints on the mechanical behaviour in the toes of accretionary prisms. *Geological Society, London, Special Publications*, *54*(1), 383–398. https://doi.org/10.1144/GSL.SP.1990.054.01.35

Karig, D. E., & Hou, G. (1992). High-stress consolidation experiments and their geologic implications. *Journal of Geophysical Research*, *97*(B1), 289–300. https://doi.org/10.1029/91JB02247

Karig, D. E., & Morgan, J. (1994). Tectonic deformation: Stress paths and strain histories. In A. Maltman (Ed.), *The geological deformation of sediments* (pp. 167–204). Dordrecht: Springer Netherlands. https://doi.org/10.1007/978-94-011-0731-0_6

Kitajima, H., Chester, F. M., & Biscontin, G. (2012). Mechanical and hydraulic properties of Nankai accretionary prism sediments: Effect of stress path. *Geochemistry, Geophysics, Geosystems*, *13*, Q0AD27. https://doi.org/10.1029/2012GC004124

Kitajima, H., & Saffer, D. M. (2012). Elevated pore pressure and anomalously low stress in regions of low frequency earthquakes along the Nankai Trough subduction megathrust. *Geophysical Research Letters*, *39*, L23301. https://doi.org/10.1029/2012GL053793

Kitajima, H., & Saffer, D. M. (2014). Consolidation state of incoming sediments to the Nankai Trough subduction zone: Implications for sediment deformation and properties. *Geochemistry, Geophysics, Geosystems*, *15*, 2821–2839. https://doi.org/10.1002/2014GC005360

Lotto, G. C., Jeppson, T. N., & Dunham, E. M. (2019). Fully coupled simulations of megathrust earthquakes and tsunamis in the Japan Trench, Nankai Trough, and Cascadia subduction zone. *Pure and Applied Geophysics*, *176*(9), 4009–4041. https://doi.org/10.1007/s00024-018-1990-y

Moore, G. F., Bangs, N. L., Taira, A., Kuramoto, S., Pangborn, E., & Tobin, H. J. (2007). Three-dimensional splay fault geometry and implications for tsunami generation. *Science*, *318*(5853), 1128–1131. https://doi.org/10.1126/science.1147195

Moore, J. C., & Saffer, D. (2001). Updip limit of the seismogenic zone beneath the accretionary prism of southwest Japan: An effect of diagenetic to low-grade metamorphic processes and increasing effective stress. *Geology*, *29*(2), 183–186. https://doi.org/10.1130/0091-7613(2001)029<0183:ULOTSZ>2.0.CO;2

Morgan, J. K., & Ask, M. V. S. (2004). Consolidation state and strength of underthrust sediments and evolution of the d'collement at the Nankai accretionary margin: Results of uniaxial reconsolidation experiments. *Journal of Geophysical Research*, *109*, B03102. https://doi.org/10.1029/2002JB002335

Rabinowitz, H. S., Savage, H. M., Skarbek, R. M., Ikari, M. J., Carpenter, B. M., & Collettini, C. (2018). Frictional behavior of input sediments to the Hikurangi Trench, New Zealand. *Geochemistry, Geophysics, Geosystems*, *19*, 2973–2990. https://doi.org/10.1029/2018GC007633

Roscoe, K. H., & Burland, J. B. (1968). On the generalised stress-strain behaviour of 'wet' clay. In J. Heyman & F. Leckie (Eds.), *Engineering plasticity* (pp. 535–609). Cambridge: Cambridge University Press.

Rutter, E., & Glover, C. (2012). The deformation of porous sandstones: Are Byerlee friction and the critical state line equivalent? *Journal of Structural Geology*, *44*, 129–140. https://doi.org/10.1016/j.jsg.2012.08.014

Saffer, D. M. (2003). Pore pressure development and progressive dewatering in underthrust sediments at the Costa Rican subduction margin: Comparison with northern Barbados and Nankai. *Journal of Geophysical Research*, *108*(B5), 2261. https://doi.org/10.1029/2002JB001787

Saffer, D. M., Silver, E. A., Fisher, A. T., Tobin, H., & Moran, K. (2000). Inferred pore pressures at the Costa Rica subduction zone: Implications for dewatering processes. *Earth and Planetary Science Letters*, *177*(3), 193–207. https://doi.org/10.1016/S0012-821X(00)00048-0

Saffer, D. M., & Tobin, H. J. (2011). Hydrogeology and mechanics of subduction zone forearcs: Fluid flow and pore pressure. *Annual Review of Earth and Planetary Sciences*, *39*(1), 157–186. https://doi.org/10.1146/annurev-earth-040610-133408

Saffer, D. M., & Wallace, L. M. (2015). The frictional, hydrologic, metamorphic and thermal habitat of shallow slow earthquakes. *Nature Geoscience*, *8*(8), 594–600. https://doi.org/10.1038/ngeo2490

Saffer, D. M., Wallace, L. M., Barnes, P. M., Pecher, I. A., Petronotis, K., LeVay, L., & the Expedition 372/375 Scientists (2019). Site U1518. In L. M. Wallace et al. (Eds.), *Hikurangi subduction margin coring, logging, and observatories* (Vol. 372B/375). College Station, TX: International Ocean Discovery Program. https://doi.org/10.14379/iodp.proc.372B375.103.2019

Screaton, E., Saffer, D., Henry, P., & Hunze, S. (2002). Porosity loss within the underthrust sediments of the Nankai accretionary complex: Implications for overpressures. *Geology*, *30*(1), 19–22. https://doi.org/10.1130/0091-7613(2002)030<0019:PLWTUS>2.0.CO;2

Skempton, A. W., & Jones, O. T. (1944). Notes on the compressibility of clays. *Quarterly Journal of the Geological Society*, *100*(1–4), 119–135. https://doi.org/10.1144/GSL.JGS.1944.100.01-04.08

Song, I., Saffer, D. M., & Flemings, P. B. (2011). Mechanical characterization of slope sediments: Constraints on in situ stress and pore pressure near the tip of the megasplay fault in the Nankai accretionary complex. *Geochemistry, Geophysics, Geosystems*, *12*, Q0AD17. https://doi.org/10.1029/2011GC003556

Tembe, S., Lockner, D. A., & Wong, T. F. (2010). Effect of clay content and mineralogy on frictional sliding behavior of simulated gouges: Binary and ternary mixtures of quartz, illite, and montmorillonite. *Journal of Geophysical Research*, *115*, B03416. https://doi.org/10.1029/2009JB006383

Wallace, L. M., & Beavan, J. (2010). Diverse slow slip behavior at the Hikurangi subduction margin, New Zealand. *Journal of Geophysical Research*, *115*, B12402. https://doi.org/10.1029/2010JB007717

Wallace, L. M., Beavan, J., Bannister, S., & Williams, C. (2012). Simultaneous long-term and short-term slow slip events at the Hikurangi subduction margin, New Zealand: Implications for processes that control slow slip event occurrence, duration, and migration. *Journal of Geophysical Research*, *117*, B11402. https://doi.org/10.1029/2012JB009489

Wallace, L. M., Saffer, D. M., Barnes, P. M., Pecher, I. A., Petronotis, K., LeVay, L., & the Expedition 372/375 Scientists (2019). Expedition 372B/375 summary. *Proceedings of the International Ocean Discovery Program* (Vol. 372B/375). https://doi.org/10.14379/iodp.proc.372B375.101.2019

Wallace, L. M., Webb, S. C., Ito, Y., Mochizuki, K., Hino, R., Henrys, S., & Sheehan, A. F. (2016). Slow slip near the trench at the Hikurangi subduction zone, New Zealand. *Science*, *352*(6286), 701–704. https://doi.org/10.1126/science.aaf2349

Williams, C. A., Eberhart-Phillips, D., Bannister, S., Barker, D. H. N., Henrys, S., Reyners, M., & Sutherland, R. (2013). Revised interface geometry for the Hikurangi subduction zone, New Zealand. *Seismological Research Letters*, *84*(6), 1066–1073. https://doi.org/10.1785/0220130035

Wood, D. (1991). *Soil behaviour and critical state soil mechanics* (pp. 1–462). Cambridge: Cambridge University Press. https://doi.org/10.1017/CBO9781139878272